INTERNATIONAL JOURNAL FOR NUMERICAL METHODS IN FLUIDS
Int. J. Numer. Meth. Fluids 2006; **50**:623–648
DOI: 10.1002/fld.1072

Finite element solution to passive scalar transport behind line sources under neutral and unstable stratification

Chun-Ho Liu*,† and Dennis Y. C. Leung‡

Department of Mechanical Engineering, The University of Hong Kong, Hong Kong, China

SUMMARY

This study employed a direct numerical simulation (DNS) technique to contrast the plume behaviours and mixing of passive scalar emitted from line sources (aligned with the spanwise direction) in neutrally and unstably stratified open-channel flows. The DNS model was developed using the Galerkin finite element method (FEM) employing trilinear brick elements with equal-order interpolating polynomials that solved the momentum and continuity equations, together with conservation of energy and mass equations in incompressible flow. The second-order accurate fractional-step method was used to handle the implicit velocity–pressure coupling in incompressible flow. It also segregated the solution to the advection and diffusion terms, which were then integrated in time, respectively, by the explicit third-order accurate Runge–Kutta method and the implicit second-order accurate Crank–Nicolson method. The buoyancy term under unstable stratification was integrated in time explicitly by the first-order accurate Euler method. The DNS FEM model calculated the scalar-plume development and the mean plume path. In particular, it calculated the plume meandering in the wall-normal direction under unstable stratification that agreed well with the laboratory and field measurements, as well as previous modelling results available in literature. Copyright © 2005 John Wiley & Sons, Ltd.

KEY WORDS: fluid turbulence; direct numerical simulation (DNS); finite element method (FEM); open-channel flow; passive scalar plume

1. INTRODUCTION

Turbulent transport under neutral and unstable stratification often occurs in geophysical flows. For example, air-pollutant transport in the atmospheric boundary layer (ABL), and contaminant transport in coastal and water environment. The transport of pollutants emitted from inhomogeneous sources, such as points or lines, is of practical interest that represents the air-pollutant-transport behaviours behind chimneys or highways placed in cross flow. In particular, the transport behaviours of passive scalar in unstably stratified turbulent flows markedly

---

*Correspondence to: Chun-Ho Liu, Department of Mechanical Engineering, 7/F, Haking Wong Building, The University of Hong Kong, Pokfulam Road, Hong Kong, China.

†E-mail: liuchunho@graduate.hku.hk

‡E-mail: ycleung@hku.hk

Received 5 February 2005
Revised 2 July 2005
Accepted 5 July 2005

differ from those in neutral ones in which the scalar plume exhibits obvious ascending and descending trajectories.

Early laboratory water tank measurements were collected to determine the turbulence structure in convective boundary layers (CBLs) [1]. In particular, the characteristic convective mixed-layer velocity scale $w^* = (g/\Theta_0 \times \langle \theta'' w'' \rangle|_{z=0}\, z_i)^{1/3}$ was developed, where $-g$ is the gravitational acceleration, Θ_0 the mean temperature of working fluid, $\langle \theta'' w'' \rangle|_{z=0}$ the heat flux at the bottom, and z_i the height of the CBL. Generally, the turbulence intensities were found to be enhanced under unstable stratification compared with those under neutral stratification. Komori *et al.* [2, 3] further confirmed experimentally the enhanced upward and downward turbulent motions under unstable stratification. Because of the increasing public concern on the air-pollutant transport in the day-time ABL, a series of laboratory measurements was performed to investigate the passive-scalar-plume behaviours under unstable stratification by using water tanks or wind tunnels [4–8]. One of the common findings in these laboratory measurements was the plume meandering in the form of ascending and descending scalar trajectories. Meanwhile, the plume behaviours for scalar emitted from point or line sources under neutral stratification were studied, respectively, by Fackrell and Robins [9] and Li and Bilger [10] using wind tunnels. Unlike that under unstable stratification, no notable plume meandering was observed under neutral stratification. These experimental results have helped to establish our basic understanding on passive-scalar-plume behaviours in the neutrally and unstably stratified ABL.

The aforementioned experimental works, though have revealed much about the scalar transport in the ABL, have been plagued by considerable technical difficulties to collect accurate measurements in some practical situations such as near-ground-level turbulence intensities and velocity–pressure correlations. On the other hand, high-resolution mathematical modelling undertaken on computers alleviated the problems. In particular, direct numerical simulation (DNS), which calculates explicitly most of the energy-carrying scales, establishes a platform for sophisticated turbulence studies by numerical approaches. DNS does not rely on the accuracy of empirical turbulence models. It calculates the flow variables to highly refined spatial resolution in a transient manner. Extensive databases are then built up for detailed statistical analyses such as the turbulent kinetic energy balance and velocity–pressure correlations.

Most of the studies available in literature have used DNS to investigate the transport behaviours of horizontally homogeneous scalar in a wide range of flow problems such as plane Couette flow [11, 12], duct flow with a free surface [13], forced-channel flow [14, 15], forced-channel flow under stratification [16], and open-channel flow [2, 3, 17–21]. In contrast, DNS studies of horizontally inhomogeneous scalar transport are relatively limited. Livescu *et al.* [22] employed a DNS model to study the behaviours of passive-scalar wake behind a line source in grid turbulence. Recently, Vrieling and Nieuwstadt [23] used DNS to investigate the interaction of the passive-scalar-plume transport between two nearby line sources in forced channel flow.

Because our understanding on the scalar-plume behaviours behind line sources in the ABL is limited yet, a DNS model utilizing the finite element method (FEM) was developed to investigate the transport behaviours of passive and inert scalar emitted from line sources at different emission heights (i.e. $z_s/H = 0, 0.25, 0.5, 0.75$, and 1.0, where H is the channel height) placed along the wall-normal extent in an open channel under neutral or unstable stratification. This paper summarizes the numerical methodology as well as the DNS results. The scalar-plume behaviours under neutral and unstable stratification are contrasted in the light of using these numerical findings from the basic physics of turbulent transport to explain the commonly observed scalar-plume behaviours in the ABL.

2. MATHEMATICAL MODEL

Incompressible turbulence of Boussinesq fluid was considered in this study. The mathematical model adopted the conservation of momentum equation

$$\frac{\partial u_i}{\partial t} + \frac{\partial}{\partial x_j} u_i u_j = -\frac{\partial p}{\partial x_i} + \frac{1}{Re} \frac{\partial^2 u_i}{\partial x_j \partial x_j} - Ri(\theta - \Theta_0)\delta_{i3} \tag{1}$$

the continuity equation

$$\frac{\partial u_i}{\partial x_i} = 0 \tag{2}$$

and the conservation of energy equation

$$\frac{\partial \theta}{\partial t} + \frac{\partial}{\partial x_i} \theta u_i = \frac{1}{Re\,Pr} \frac{\partial^2 \theta}{\partial x_i \partial x_i} \tag{3}$$

Equations (1)–(3) are expressed in tensor notation and the usual summation convention on repeated indices (i and j) is employed. All the variables are appropriately made dimensionless by the channel height H (reference length scale), the mean-flow speed at the top of the channel U (reference velocity scale), and the reference time scale T $(=H/U)$. The variables x_i are the Cartesian coordinates ($i = 1, 2$, and 3 representing the streamwise x, spanwise y, and wall-normal z directions, respectively), t is the time, u_i are the velocity components ($i = 1, 2$, and 3 representing the velocity components in the streamwise u, spanwise v, and wall-normal w directions, respectively), p is the kinematic pressure, θ is the temperature, and δ_{ij} is the Kronecker symbol. The dimensionless parameters are the Reynolds number Re $(= UH/v)$, the Prandtl number Pr $(= v/\mathscr{K})$, and the Richardson number Ri $(= -g \times H/\Theta_0 \times \Delta\Theta/U^2)$. Here, v is the kinematic viscosity, $\mathscr{K}$ is the thermal diffusivity, and $\Delta\Theta$ is the mean temperature difference across the channel in wall-normal direction (reference temperature scale). With the simulated flow field, the scalar transport is calculated by the mass-conservation equation of passive and inert scalar

$$\frac{\partial \phi}{\partial t} + \frac{\partial}{\partial x_i} \phi u_i = \frac{1}{Re\,Sc} \frac{\partial^2 \phi}{\partial x_i \partial x_i} \tag{4}$$

where ϕ is the scalar mixing ratio normalized by the scalar source strength Φ (reference scalar mixing ratio scale), Sc $(= v/\kappa)$ is the Schmidt number, and κ is the mass diffusivity.

3. COMPUTATIONAL INFORMATION

3.1. Numerical methodology

Equations (1)–(4) were solved by the three-dimensional (3D) FEM in a transient manner. The implicit dependence in-between velocity and pressure in incompressible flow was decoupled by the second-order accurate fractional-step method. The equal-order FEM with trilinear interpolating polynomials were used to discretize the velocity components u_i, pressure p, temperature θ, and scalar mixing ratio ϕ in the spatial domain. The detailed numerical methodology is described in this section.

3.1.1. Fractional-step method. A second-order accurate fractional-step method was used to decouple the momentum equations in accordance with

$$\frac{\widehat{u}_i - u_i^t}{\Delta t} = -\mathrm{N}(u_i^t, u_j^t) \tag{5}$$

$$\frac{\widetilde{u}_i - \widehat{u}_i}{\Delta t} = -\frac{\partial p^t}{\partial x_i} + \frac{1}{Re}\frac{\partial^2}{\partial x_j \partial x_j}\left(\frac{\widetilde{u}_i + u_i^t}{2}\right) - Ri(\theta^t - \Theta_0)\delta_{i3} \tag{6}$$

$$\frac{\check{u}_i - \widetilde{u}_i}{\Delta t} = \frac{\partial p^t}{\partial x_i} \tag{7}$$

and

$$\frac{u_i^{t+\Delta t} - \check{u}_i}{\Delta t} = -\frac{\partial p^{t+\Delta t}}{\partial x_i} \tag{8}$$

Here Δt is the time-step increment, $\widetilde{u}_i$, $\widehat{u}_i$, and $\check{u}_i$ are the intermediate velocity components that do not necessarily satisfy the continuity, and $\mathrm{N}(u_i^t, u_j^t) = \partial/\partial x_j\,(u_i^t u_j^t)$ is the advection term. The superscript implies that the variables are calculated at time t. Summing up Equations (5)–(8) retrieves the velocity–pressure coupled momentum equation. Instead of $u_i^{t+\Delta t}$ and $p^{t+\Delta t}$, using $\widetilde{u}_i$ and p^t in Equation (6) is a second-order accurate approximation of Equation (1) because $u_i^{t+\Delta t} - \widetilde{u}_i = \Delta t(\partial p^t - \partial p^{t+\Delta t})/\partial x_i = \mathcal{O}(\Delta t^2)$ [24, 25]. Under unstable stratification, the buoyancy term was solved explicitly by the first-order accurate Euler method.

The advection and diffusion terms in the energy-conservation equation were segregated by the fractional-step method as well. The mathematical procedures consisted of

$$\frac{\widehat{\theta} - \theta^t}{\Delta t} = -\mathrm{N}(\theta^t, u_i^t) \tag{9}$$

and

$$\frac{\theta^{t+\Delta t} - \widehat{\theta}}{\Delta t} = \frac{1}{Re\,Pr}\frac{\partial^2}{\partial x_i \partial x_i}\left(\frac{\theta^{t+\Delta t} + \theta^t}{2}\right) \tag{10}$$

where $\widehat{\theta}$ is the intermediate temperature. Due to the similar nature of the transport equations, the scalar mixing ratio was also solved by the fractional-step method. The variables θ and Pr in Equations (9) and (10) were then replaced by ϕ and Sc, respectively.

The aforementioned fractional-step methods not only decoupled the velocity components and pressure but also segregated the advection and diffusion terms in the temporal domain. The diffusion terms were integrated implicitly in time by the second-order accurate Crank–Nicolson (CN) method. In view of their non-linear nature, the advection terms were integrated explicitly in time by the third-order accurate Runge–Kutta (RK) method. Another benefit of the RK method is its large Courant–Fredrichs–Lewy (CFL) number because the mesh spacing (in the streamwise and wall-normal directions) near the line sources was small (see Table I).

Table I. Simulation parameters adopted in the current DNS FEM model expressed in global and wall units.

	Simulation parameters			
	Global units		Wall units	
	Neutral	Unstable	Neutral	Unstable
Domain size	$L_x \times L_y \times L_z = 12H \times 4H \times H$		$L_x^+ \times L_y^+ \times L_z^+ = 2160 \times 720 \times 180$	
Number of elements	$N_x \times N_y \times N_z = 448 \times 64 \times 96 = 2\,752\,512$			
Reference velocity scale	$U = 0.73$	$U = 0.54$	$u_\tau = 180$	
Reynolds number	$Re = 2900$	$Re = 2200$	$Re_\tau = 180$	
Prandtl number	$Pr = 0.72$			
Schmidt number	$Sc = 0.72$			
Richardson number	N/A	$\mathrm{Ri} = -0.20$	N/A	
Convective velocity scale	N/A	$w^* = 0.20$	N/A	
	$0.011H \leqslant \Delta x \leqslant 0.065H$		$1.98 \leqslant \Delta x^+ \leqslant 11.70$	
Mesh spacing	$\Delta y = 0.063H$		$\Delta y^+ = 11.25$	
	$0.0040H \leqslant \Delta z \leqslant 0.024H$		$0.72 \leqslant \Delta z^+ \leqslant 4.39$	
Time step increment	$\Delta t = 0.01T$		$\Delta t^+ = 8.1$	
CFL number	$0.11 \leqslant \mathrm{CFL} \leqslant 0.70$			

The superscript + represents that the simulation parameters are expressed in wall units. L_x, L_y and L_z are, respectively, the extents in the streamwise, spanwise, and wall-normal directions of the spatial domain. N_x, N_y, and N_z are, respectively, the number of elements in the streamwise, spanwise, and wall-normal directions.

3.1.2. Finite element formulation. The Galerkin FEM was used to discretize the mathematical model in the spatial domain Ω. A dependent variable $\psi(x_i, t)$ was approximated by a linear combination of the (Lagrange) interpolating polynomial $\varphi(x_i)$ and the nodal values of the variable $\psi_\gamma(t)$ in the form of

$$\psi(x_i, t) = \sum_{\gamma=1}^{nde} \varphi_\gamma(x_i)\psi_\gamma(t) \tag{11}$$

where *nde* is the number of node points in Ω and the subscript γ is the nodal index. As an equal-order FEM was used, the velocity components, pressure, temperature, and scalar mixing ratio were approximated by Equation (11) using the same trilinear interpolating polynomial defined on brick elements.

The Galerkin method was used to construct the weighted residual formulation in which the weighting function was equal to the interpolating polynomial. The weak formulation of the mathematical model was derived by multiplying Equations (5)–(8) with the weighting function and then integrated over the spatial domain. These mathematical procedures yielded the following equations in matrix notation:

$$\int_\Omega \frac{\varphi_\alpha \varphi_\beta}{\Delta t}\,\mathrm{d}\Omega\, \widehat{u}_{i_\beta} = \int_\Omega \frac{\varphi_\alpha \varphi_\beta}{\Delta t}\,\mathrm{d}\Omega\, u_{i_\beta}^t - \int_\Omega \varphi_\alpha\, \mathrm{N}(u_i^t, u_j^t)\,\mathrm{d}\Omega \tag{12}$$

$$\begin{aligned}\int_\Omega \left(\frac{\varphi_\alpha\varphi_\beta}{\Delta t}+\frac{1}{2\,Re}\frac{\partial\varphi_\alpha}{\partial x_j}\frac{\partial\varphi_\beta}{\partial x_j}\right)\mathrm{d}\Omega\,\tilde{u}_{i_\beta}
&=\int_\Omega \frac{\varphi_\alpha\varphi_\beta}{\Delta t}\,\mathrm{d}\Omega\,\hat{u}_{i_\beta}-\frac{1}{2\,Re}\int_\Omega \frac{\partial\varphi_\alpha}{\partial x_j}\frac{\partial\varphi_\beta}{\partial x_j}\,\mathrm{d}\Omega\,u^t_{i_\beta}\\
&\quad-\int_\Omega \varphi_\alpha\frac{\partial\varphi_\beta}{\partial x_i}\,\mathrm{d}\Omega\,p^t_\beta-\delta_{i3}Ri\int_\Omega \varphi_\alpha\varphi_\beta\,\mathrm{d}\Omega(\theta^t_\beta-\Theta_0)\end{aligned}\tag{13}$$

$$\int_\Omega \frac{\varphi_\alpha\varphi_\beta}{\Delta t}\,\mathrm{d}\Omega\,\check{u}_{i_\beta}=\int_\Omega \frac{\varphi_\alpha\varphi_\beta}{\Delta t}\,\mathrm{d}\Omega\,\tilde{u}_{i_\beta}+\int_\Omega \varphi_\alpha\frac{\partial\varphi_\beta}{\partial x_i}\,\mathrm{d}\Omega\,p^t_\beta\tag{14}$$

and

$$\int_\Omega \frac{\varphi_\alpha\varphi_\beta}{\Delta t}\,\mathrm{d}\Omega\,u^{t+\Delta t}_{i_\beta}=\int_\Omega \frac{\varphi_\alpha\varphi_\beta}{\Delta t}\,\mathrm{d}\Omega\,\check{u}_{i_\beta}-\int_\Omega \varphi_\alpha\frac{\partial\varphi_\beta}{\partial x_i}\,\mathrm{d}\Omega\,p^{t+\Delta t}_\beta\tag{15}$$

where the subscripts α and β are indices of matrix components. The integration by parts and the divergence theorem had been employed in deriving Equations (13) from (6).

The calculation of the divergence-free velocity $u_i^{t+\Delta t}$ by Equation (15) required the updated pressure $p^{t+\Delta t}$ which was calculated by considering the Galerkin weighted residual formulation of the continuity Equation (2) in its integral form

$$\int_\Omega \varphi\frac{\partial u_i^{t+\Delta t}}{\partial x_i}\,\mathrm{d}\Omega=0\tag{16}$$

Invoking the integration by parts and the divergence theorem, Equation (16) was rewritten as

$$\int_\Omega \frac{\partial\varphi}{\partial x_i}u_i^{t+\Delta t}\,\mathrm{d}\Omega=\oint_\Gamma \varphi u_i^{t+\Delta t}n_i\,\mathrm{d}\Gamma\tag{17}$$

where Γ is the surface of Ω and n_i is the unit normal to Γ. Substituting Equation (8) into (17) led to the Poisson-type pressure equation

$$\int_\Omega \frac{\partial\varphi_\alpha}{\partial x_i}\frac{\partial\varphi_\beta}{\partial x_i}\,\mathrm{d}\Omega\,p^{t+\Delta t}_\beta=\frac{1}{\Delta t}\left(\int_\Omega \frac{\partial\varphi_\alpha}{\partial x_i}\varphi_\beta\,\mathrm{d}\Omega\,\check{u}_{i_\beta}-\oint_\Gamma \varphi_\alpha u_i^{t+\Delta t}n_i\,\mathrm{d}\Gamma\right)\tag{18}$$

With the intermediate velocity components $\check{u}_i$, Equation (18) was then solved for the updated nodal pressure $p_\beta^{t+\Delta t}$. Because of the periodic and Dirichlet boundary conditions adopted along Γ, the surface integral vanished in the DNS FEM model.

The global spatial domain Ω was discretized into non-overlapping elements Ω_e and so were the global integrals expressed in Equations (12)–(15), and (18). The integrals for individual element were calculated numerically by Gauss quadrature with three Gaussian points in each coordinate direction. The aforementioned FEM procedures led to several systems of linear equations. Because of the structure of the mass and diffusion matrices, and the explicit RK solvers employed in solving the advection terms, the coefficient matrices of all the linear-equation systems were symmetric and positive definite. The systems of linear equations were then solved by the conjugate gradient (CG) iteration with the Jacobian preconditioner [26] for the nodal velocity $u_{i_\alpha}^{t+\Delta t}$, pressure $p_\alpha^{t+\Delta t}$, temperature $\theta_\alpha^{t+\Delta t}$, and scalar mixing ratio $\phi_\alpha^{t+\Delta t}$.

3.2. Parallel implementation

The DNS FEM code employed a mixed approach for parallelism. Its data structure made use of the non-overlapping domain decomposition in which each processor only stored the parameters in its subdomain. The computational load was distributed evenly to each processor by defining a Cartesian virtual topology prior to the computation. Numerous matrix operations were involved in the DNS FEM model. The data parallelism was used in these matrix operations in which each processor handled only the local operations in its subdomain. Collective communication and communication between nearest neighbouring processors were used to account for the contribution from different subdomains. The detailed parallel implementation of the DNS FEM code was discussed elsewhere [27, 28].

The computation was conducted on the Linux PC clusters maintained by the Computer Centre of the University of Hong Kong. The Linux PC clusters totally consisted of 32 nodes in which each node had dual Intel P III 1 GHz processors. The DNS FEM model used 8 nodes (16 processors). Each node was equipped with a HP ProLiant DL 360 rack-mount-server mother board, 256 kB of cache, and 2 GB of memory. The nodes were connected by Fast Ethernet. The operation system was Red Hat Linux 7.2 with 2.4.7-10 smp kernel. The DNS FEM model was coded in FORTRAN 90 and the Portland Group's PGF90 compiler was used. The MPICH library was used for inter-processor communication. The Basis Linear Algebra Subprograms (BLAS) library was used to handle the matrix operations whenever possible. The parallel performance of the DNS FEM code was discussed elsewhere [29, 30].

3.3. Computational domain and boundary conditions

In this study, the spatial domain was a rectangular channel of size $12H$ (streamwise) $\times 4H$ (spanwise) $\times H$ (wall-normal) as sketched in Figure 1. The mean flow was driven by a constant background pressure gradient ΔP. A non-slip rigid wall with zero velocity ($u_i = 0$) and constant temperature ($\Delta\Theta/2$) was assumed at the bottom of the channel. A shear-free boundary with no deformation, zero wall-normal flow ($\partial u/\partial z = \partial v/\partial z = w = 0$), and constant temperature ($-\Delta\Theta/2$) was assumed at the top of the channel. This flow configuration was a good representation of a free surface if the wall-normal deformation was negligible compared

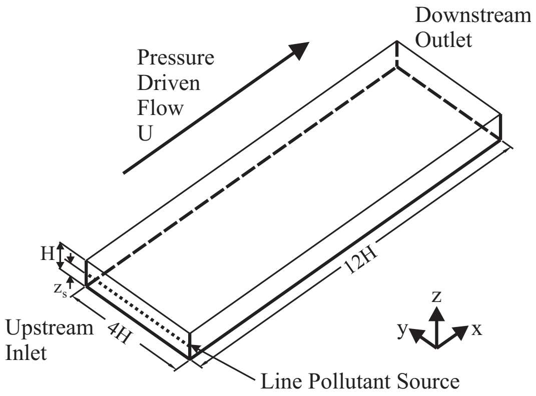

Figure 1. Schematic diagram of the spatial domain Ω adopted in the DNS FEM model.

with the channel height at a low Reynolds number [20]. The temperature at the lower wall was hotter than that at the upper shear-free boundary. Hence, the buoyancy was opposite to the gravity and the channel was unstably stratified. The neutral stratification was simply simulated by switching off the buoyancy term. Periodic boundary conditions for flow and temperature calculation were assumed in the horizontal directions.

Passive and chemically inert scalar, which was used to account for the pollutant transport, was emitted into the channel through hypothetical line sources placed in the cross flow parallel to the spanwise direction at $x/H = 0$. Five emission heights at $z_s/H = 0, 0.25, 0.5, 0.75$, and 1 were adopted. These scalar sources were simulated in the form of Dirichlet boundary conditions of constant scalar source strength Φ. The upstream inlet was free of scalar ($\phi = 0$). At the downstream outlet an open boundary condition ($\partial\phi/\partial t + u\,\partial\phi/\partial x = 0$) was assumed where the scalar was removed from the channel with negligible distortion or reflection. A periodic boundary condition in the spanwise direction, together with zero-gradient boundary conditions at the wall and the shear-free boundary for the scalar were assumed.

The DNS was started from the analytical solution to laminar open-channel flow, and heat and mass transfer problems. The turbulence was triggered by small random perturbations imposed on the laminar temperature field. Under unstable stratification, as the buoyancy term was kept, the turbulence was developing for 100 dimensionless time unit until it reached statistically steady state. On the other hand, under neutral stratification, on top of the randomly perturbed temperature field, the buoyancy term was switched on for 3 dimensionless time unit to initiate the turbulence development. Afterward, the buoyancy term was switched off and the turbulence continued to develop for 100 dimensionless time unit until statistically steady state. For both neutral and unstable stratification, after the turbulence-development stage, the results were collected for another 100 dimensionless time unit for analyses.

The detailed computation parameters are tabulated in Table I. The mesh spacing in the horizontal directions was comparable to those used in other DNS studies. The mesh spacing in the wall-normal direction in the near-wall region was definitely coarser than that adopted in the forced channel turbulence ($0.05 \leqslant \Delta z^+ \leqslant 4.4$) [31]. Instead, it was close to that adopted in the turbulent plane Couette flow ($0.7 \leqslant \Delta z^+ \leqslant 3.9$) [32]. Hence, the DNS FEM model was capable of comparing the plume meandering behaviours, at least qualitatively, under neutral and unstable stratification. In fact, its reliability was also assessed in an extensive model validation exercise to be presented in the next section.

4. RESULTS AND DISCUSSIONS

This study focused on comparing the scalar-plume-transport behaviours under neutral and unstable stratification. In the following discussion, statistical means denoted by parenthesis $\langle\ \rangle$ represented spatial (in the homogeneous directions) and temporal averages. Thus, the statistical means of fluid turbulence were averaged in both streamwise and spanwise directions. The statistical means of scalar variables were averaged in the spanwise direction only.

4.1. Fluid turbulence

Figure 2 compares the wall-normal profiles of the mean-flow speed $\langle u\rangle$ in neutrally and unstably stratified open channels. Under neutral stratification, the DNS-calculated mean-flow

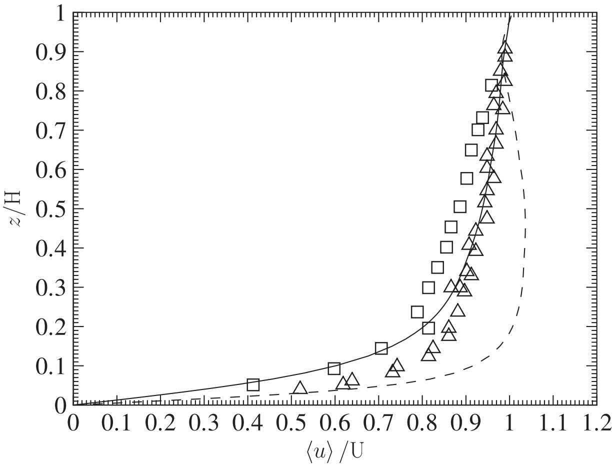

Figure 2. Wall-normal profiles of mean flow speed $\langle u\rangle/U$ in neutrally — and unstably ($Ri = -0.2$) ––– stratified open channels calculated by the DNS FEM model. Also shown are the laboratory measurements collected under neutral □ [2] and unstable ($Ri = -0.049$) △ [3] stratification.

speed showed small overprediction ($\leqslant 5\%$) compared with laboratory measurements [2]. It increased rapidly from zero at the wall to $0.8U$ at $z/H = 0.2$ in the wall-normal direction. Its development slowed down thereafter and converged gradually to the shear-free-boundary speed.

On the other hand, under unstable stratification, enhanced turbulent mixing due to buoyancy led to a broad range ($0.2 \leqslant z/H \leqslant 0.8$) of relatively constant mean-flow speed ($\approx U$) in the centre core of the channel. This broad mean-flow speed in turn led to a more rapidly increasing wall-normal profile of mean-flow speed in the near-wall region. The mean-flow speed increased from zero at the wall to U at $z/H = 0.2$. In the upper part of the channel, it decreased slightly and developed a mild local minimum of mean-flow speed ($0.98U$) at $z/H = 0.85$. Also shown in Figure 2 is the laboratory-measured wall-normal profile of mean-flow speed in an unstably stratified open channel at $Ri = -0.049$ [3]. Generally, increasing the unstable stratification, because of the enhanced turbulent transport, developed a broad constant of mean-flow speed in the centre core of the channel. As the Richardson number for the present DNS FEM model was greater than that adopted in the laboratory experiment [3] by more than 4 times, the DNS-calculated mean-flow speed was greater than the laboratory-measured one and so was the centre-core broad maximum. Nonetheless, the DNS FEM model predicted the general behaviours of mean-flow speed in neutral and unstable stratification.

The calculated wall-normal profiles of the root-mean-square (RMS) velocity fluctuations $\langle u_i'' u_i''\rangle^{1/2}$ under neutral and unstable stratification are contrasted in Figure 3. Under neutral stratification, the streamwise RMS velocity fluctuation developed rapidly from zero at the wall to a local maximum ($\langle u'' u''\rangle^{1/2}/U = 0.18$) at $z/H = 0.1$. Afterward, it decreased to $0.06U$ at the shear-free boundary. The spanwise RMS velocity fluctuation also increased rapidly in the near-wall region that developed from zero at the wall to $\langle v'' v''\rangle^{1/2}/U = 0.05$ at $z/H = 0.15$. It was then kept fairly constant at this value for most of the channel height ($0.15 \leqslant z/H \leqslant 1$). Due to the velocity boundary conditions adopted in the DNS FEM model, the wall-normal

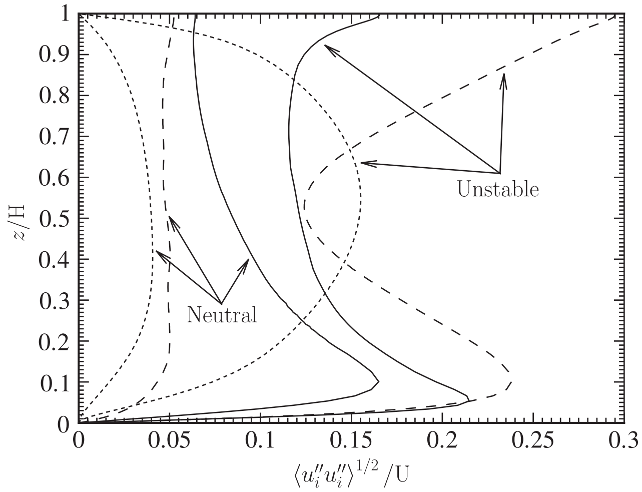

Figure 3. Wall-normal profiles of RMS streamwise $\langle u''u''\rangle^{1/2}/U$ —, spanwise $\langle v''v''\rangle^{1/2}/U$ – – –, and wall-normal $\langle w''w''\rangle^{1/2}/U$ ······ velocity fluctuation calculated by the DNS FEM model in neutrally and unstably stratified open channels.

RMS velocity fluctuation at the wall and the shear-free boundary was zero. Its maximum $\langle w''w''\rangle^{1/2}/U = 0.04$ resided at $z/H = 0.38$.

Under unstable stratification, heating at the bottom of the channel resulted in significant increase in turbulence kinetic energy than did under neutral stratification (Figure 3). The streamwise RMS velocity fluctuation developed from zero at the wall to a local maximum ($\langle u''u''\rangle^{1/2}/U = 0.22$) at $z/H = 0.06$. Afterward, it decreased gradually in the wall-normal direction until the upper part of the channel. It increased again within the region close to the top of the channel ($0.9 \leqslant z/H \leqslant 1$) and eventually arrived $0.18U$ at the shear-free boundary. The spanwise RMS velocity fluctuation developed from zero at the wall to a local maximum ($\langle v''v''\rangle^{1/2}/U = 0.24$) at $z/H = 0.1$. Because of the buoyancy, it also developed another local maximum ($\langle v''v''\rangle^{1/2}/U = 0.3$) at the shear-free boundary which was even greater than its streamwise counterpart. In-between these maxima was a local minimum near the channel centre ($\langle v''v''\rangle^{1/2}/U = 0.13$ at $z/H = 0.53$). A local maximum of wall-normal RMS velocity fluctuation ($\langle w''w''\rangle^{1/2}/U = 0.15$) was developed at the channel centre whose location was higher than that under neutral stratification discussed above.

4.2. Mean plume path

The mean plume path $\bar{z}$ of the scalar, which is calculated by

$$\bar{z}(x) = \frac{\int_0^H \langle \phi(x,z)\rangle z \, \mathrm{d}z}{\int_0^H \langle \phi(x,z)\rangle \, \mathrm{d}z} \tag{19}$$

exhibited obviously different plume behaviours under neutral and unstable stratification. It was because well mixing was being developed in the streamwise direction, the mean plume paths for the scalar emitted under neutral stratification converged gradually from the emission heights toward the channel centre ($z/H = 0.5$, Figure 4(a)). On the contrary, meandering of

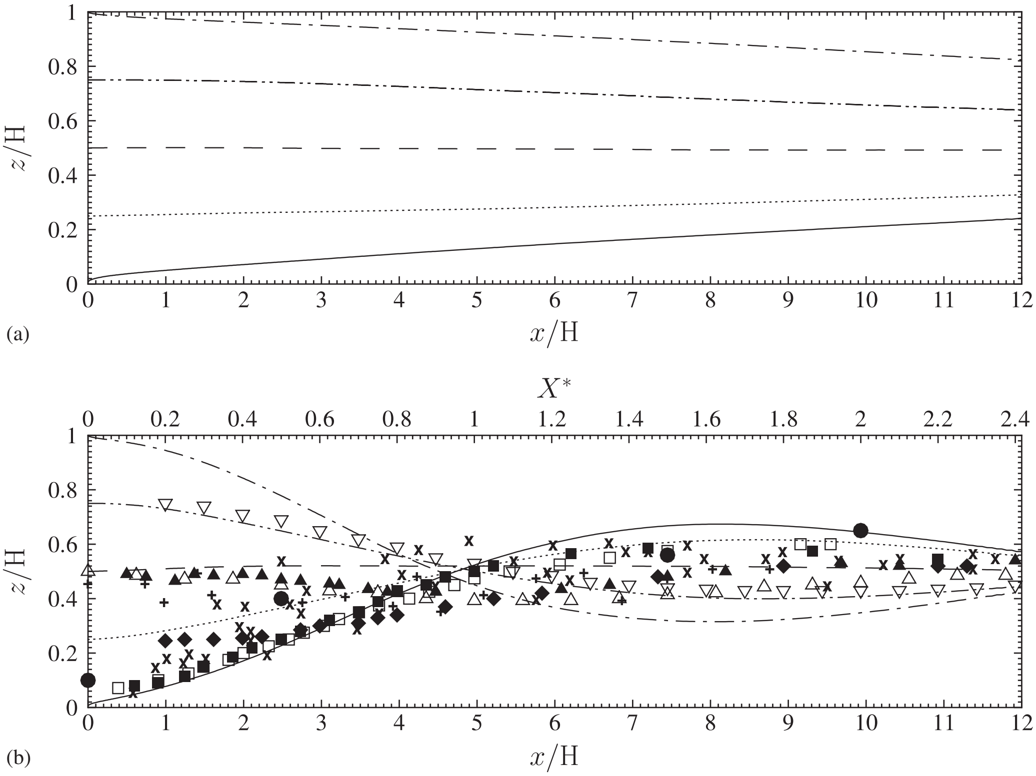

Figure 4. Mean plume paths $\bar{z}/H$ plotted as functions of streamwise distance x/H in (a) neutrally and (b) unstably stratified open channels. The DNS-calculated results for scalar emitted at $z_s/H =$: 0 —, 0.25 ······, 0.5 – – –, 0.75 ··—·—, and 1 ·—·—. Laboratory measurements for scalar emitted at $z_s/H =$: 0.067 ■ [4] and ● [7], 0.25 ♦ [5], and 0.5 ▲ [6]. Field measurements for scalar emitted at $z_s/H =$: 0 × and 0.5 + [33]. Second-order closure turbulence model results for scalar emitted at $z_s/H = 0.75$ ▽ [34]. LES results for scalar emitted at $z_s/H =$: 0 □ and 0.5 △ [35].

scalar, in the form of plume rise and descent in the wall-normal direction, was observed under unstable stratification (Figure 4(b)). To demonstrate the accuracy of the DNS FEM model, the laboratory measurements [4–7], field measurements [33], second-order-closure-modelling results [34], and large-eddy-simulation (LES) results [35] under unstable stratification are also shown.

As shown, the scalar emitted in the lower part of the unstably stratified channel was carried aloft to the upper part. The scalar emitted at the bottom (i.e. $z_s/H = 0$) exhibited the largest plume rise amongst the emission heights tested. It rose rapidly right after emission, passed through the channel centre at $x/H = 4.8$, and reached its maximum mean plume height ($\bar{z}/H = 6.8$) at $7.7 \leqslant x/H \leqslant 8.5$. Afterward, it descended and converged gradually toward the channel centre at the downstream outlet. Within the early plume development in the lower path of the channel, the DNS-calculated mean plume path followed closely the laboratory-measured values for $z_s/H = 0.067$ [4]. In the upper part of the channel (i.e. the far field of the scalar plume), the measured mean plume path [4] rose to $\bar{z}/H = 0.6$ at $7.2 \leqslant x/H \leqslant 8.4$.

The DNS-calculated maximum mean plume path was higher than the measured value by about 13%.

The DNS-calculated mean plume paths under unstable stratification were also compared with field measurements (Figure 4(b)). The mean plume path measured in a CBL was sparse [33]. Its elevation was higher than the DNS-calculated value within the early plume development ($0 \leqslant x/H \leqslant 6$) but lower thereafter. The field-measured maximum mean plume path was $\bar{z}/H = 0.6$ at $x/H = 5$. It occurred earlier than that obtained from the DNS FEM model or the laboratory water tank experiment [4]. The sample size of another set of laboratory measurement was limited and the data points were sparse [7]. Generally, the DNS-calculated mean plume path fell within these sparse data points though the laboratory measurement showed slightly higher mean plume path within the early plume development.

Since the LES model [35] generally followed the parameters adopted in the convective water tank experiment [4], their mean plume path were close to each other throughout the streamwise extent. On the other hand, though different simulation parameters had been employed in the LES [35] and the present DNS FEM models, their calculated mean plume paths were close to each other within the early plume development ($0 \leqslant x/H \leqslant 5$). Afterward, the LES-calculated maximum mean plume path ($\bar{z}/H = 0.6$ at $9.2 \leqslant x/H \leqslant 9.5$) was lower than the DNS-calculated value by about 10%.

A rapid plume rise was also observed for the scalar emitted at $z_s/H = 0.25$ in which the mean plume path passed through the channel centre at $x/H = 5$ (Figure 4(b)). Even the emission height was elevated by 25%, it showed a lower maximum mean plume path ($\bar{z}/H = 0.6$ at $8 \leqslant x/H \leqslant 9$) than that of $z_s/H = 0$. Afterward, it converged gradually toward the channel centre as the scalar was being mixed in the streamwise direction. The DNS-calculated mean plume path for $z_s/H = 0.25$ was higher than that measured in the convective water tank experiment [5] throughout the streamwise extent. The laboratory-measured mean plume path passed through the channel centre at $x/H = 7.5$ before reaching its maximum ($\bar{z}/H = 0.6$ at $x/H = 9$), which was lower than the DNS-calculated value by almost 20%.

As calculated by the DNS FEM model, the scalar emitted at the channel centre ($z_s/H = 0.5$) did not show obvious plume meandering (Figure 4(b)). Instead, it travelled almost horizontally throughout the streamwise extent. Whereas, the convective water tank experiment [6] showed a mild plume descent right after emission whose minimum mean plume path was $\bar{z}/H = 0.44$ at $3.6 \leqslant x/H \leqslant 4.5$. The mean plume path then ascended slightly before converging toward the channel centre. The field measurements in a CBL were sparse [33] whose mean plume path covered a wider range ($0.36 \leqslant \bar{z}/H \leqslant 0.6$) compared with those measured by the laboratory convective water tank experiment [6] or those calculated by the DNS FEM model. Also shown in Figure 4(b) was the LES-calculated mean plume path [35] that followed quite closely the laboratory-measured value [6]. However, it descended slightly deeper than that of the laboratory measurement to $\bar{z}/H = 0.4$ at $5 \leqslant x/H \leqslant 5.6$.

The DNS-calculated mean plume path showed that the scalar emitted at the upper part of the unstably stratified open channel generally descended right after emission. The scalar emitted at $z_s/H = 0.75$ followed the descending mean plume path and passed through the channel centre at $x/H = 5$. It continued descending to its minimum mean plume path ($\bar{z}/H = 0.4$ at $8 \leqslant x/H \leqslant 10$) before converged gradually toward the channel centre with increasing downstream distance. The mean plume path calculated by the second-order closure turbulence model [34] was comparable to that of the DNS FEM model. Its minimum mean plume path was slightly higher ($\bar{z}/H = 4.4$ at $8 \leqslant x/H \leqslant 10$) than the DNS-calculated one.

The DNS FEM outputs showed that the plume descent for scalar emitted at $z_s/H = 1$ was the deepest amongst the emission heights tested. The descending scalar plume passed through the channel centre at $x/H = 4.5$ before reaching its minimum mean plume path ($\bar{z}/H = 0.3$) at $7.5 \leqslant x/H \leqslant 9$. Analogous to the scalar-plume behaviour for other emission heights, the scalar was being mixed and the mean plume path gradually converged toward the channel centre in the streamwise direction thereafter.

4.3. Dispersion coefficient

The mean plume coverage and the scalar mixing in the crosswind (wall-normal) direction can be quantified by the dispersion coefficient σ_z which is defined as

$$\sigma_z^2(x) = \frac{\int_0^H \langle \phi(x,z) \rangle [z - \bar{z}(x)]^2 \, dz}{\int_0^H \langle \phi(x,z) \rangle \, dz} \tag{20}$$

The dispersion coefficients for different emission heights in neutrally and unstably stratified channels were expressed as functions of downstream distance, respectively, in Figures 5(a) and (b).

Under neutral stratification, the dispersion coefficients for different emission heights developed gradually in the streamwise direction (Figure 5(a)). Because of the limited computational resources and lengthy computation time, one of the weaknesses of the DNS FEM calculation was the limited streamwise coverage, i.e. $12H$ which was not long enough for the scalar to achieve completely well-mixed condition. Additional DNS calculation for longer streamwise extent ($30H$) is currently in progress so as to investigate the scalar-transport behaviours after well-mixed condition. The maximum dispersion coefficients calculated by the DNS FEM model were in the range $0.15 \leqslant \sigma_x/H \leqslant 0.25$ locating at the downstream outlet. Throughout the streamwise extent of the channel, the dispersion coefficients for the scalar emitted at $z_s/H = 0.25$ and 0.5, which were the largest ones amongst the emission heights tested, were very close to each other whose differences were less than 5%. Their comparable values were mainly due to the broad-range of relatively constant wall-normal RMS velocity fluctuation $\langle w''w'' \rangle^{1/2}$ at these levels of the channel (Figure 3). The dispersion coefficient for the scalar emitted at $z_s/H = 0.75$ was smaller (about 25%) than those emitted at $z_s/H = 0.25$ and 0.5. This reduction was mainly due to the smaller wall-normal RMS velocity fluctuation that weakened the scalar mixing together with the plume coverage. At the bottom of the channel, because of the tiny wall-normal RMS velocity fluctuation in the near-wall region, the dispersion coefficient for the scalar emitted at $z_s/H = 0$ was smaller than those emitted in the centre core of the channel ($z_s/H = 0.25, 0.5$, and 0.75). Finally, the dispersion coefficient for the scalar emitted at $z_s/H = 1$ was the smallest amongst the emission heights tested. Its noticeable reduction was attributed by the large mean flow together with the small wall-normal RMS velocity fluctuation near the shear-free boundary.

Unlike the gradually developing scalar-plume coverage under neutral stratification, the dispersion coefficients for the scalar transport under unstable stratification increased rapidly right after emission from $\sigma_z/H = 0$ to 0.25–0.3 after a downstream distance $x/H \leqslant 5$ for the emission heights tested (Figure 5(b)). Their values were quite constant thereafter that signified the well-mixed conditions under unstable stratification (compared with those under neutral stratification). Because of the broad constant mean-flow speed and wall-normal RMS velocity fluctuation in the centre core of the unstably stratified channel, the dispersion coefficients for

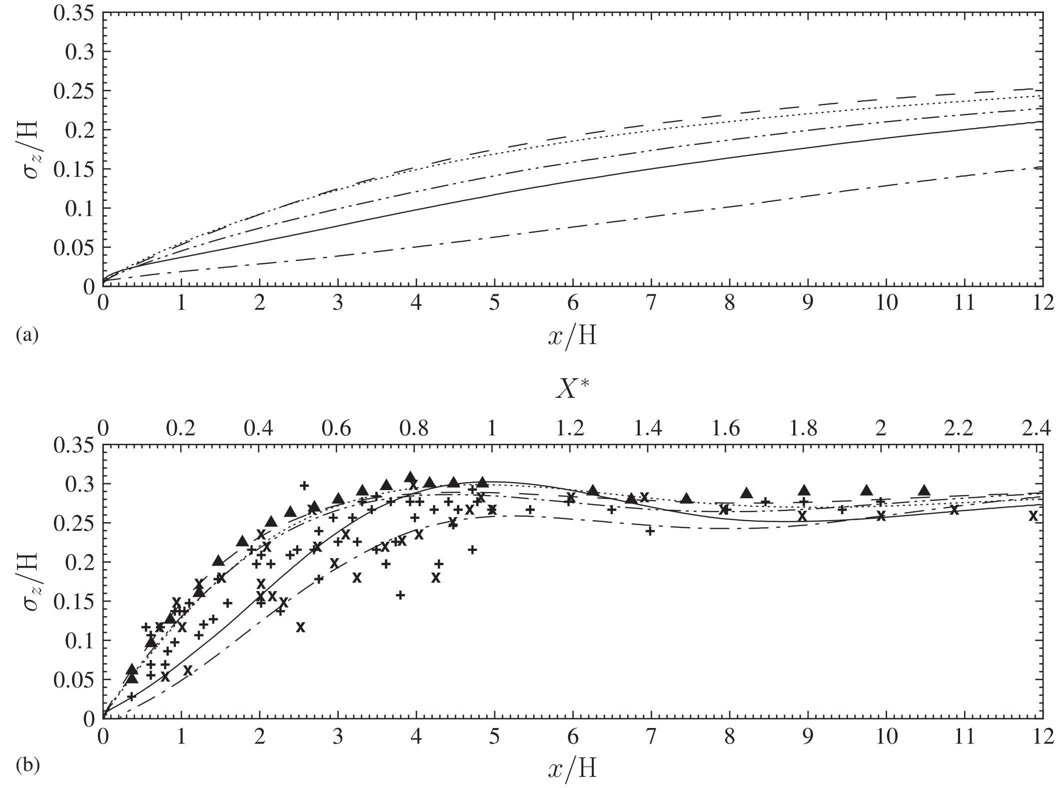

Figure 5. Dispersion coefficients σ_z/H plotted as functions of streamwise distance x/H in (a) neutrally and (b) unstably stratified open channels. The DNS-calculated results for scalar emitted at $z_s/H =$: 0 ——, 0.25 ······, 0.5 – – –, 0.75 —·——·—, and 1 —·——·—. Laboratory measurements for scalar emitted at $z_s/H =$ 0.5 ▲ [6]. Field measurements for scalar emitted at $z_s/H =$: 0 × and 0.5 + [33].

the scalar emitted at $z_s/H = 0.25, 0.5$, and 0.75 were close to each other after reaching their maximum values. In view of the smaller wall-normal RMS velocity fluctuation, the dispersion coefficients for the scalar emitted at the bottom and top of the channel were smaller than those emitted in the centre core of the channel within the early plume development ($x/H \leqslant 4$). However, the plume meandering under unstable stratification, which also helped to mix the scalar, increased the crosswind scalar dispersion and plume coverage as well. As a result, the dispersion coefficients for the emission heights tested were of comparable magnitudes in the far field of the scalar plume.

Figure 5(b) also showed the accuracy of the DNS FEM model by comparing with the results available in literature. The DNS-calculated dispersion coefficients agreed well with the measurements collected in the convective water tank experiment for $z_s/H = 0.5$ [6]. The smaller wall-normal RMS velocity fluctuation in the lower near-wall region led to a reduced dispersion coefficient for the scalar emitted at $z_s/H = 0$. The rapid plume rise carried the mean plume path aloft from the lower part to the centre core and then the upper part of the channel. This rapid plume rise also increased the dispersion coefficient to $\sigma_z/H = 0.3$ at $x/H = 5$ which was the largest amongst the emission heights tested. The field-measured dispersion coefficients for the scalar emitted at $z_s/H = 0$ and 0.5 were quite scattering [33], nonetheless, the DNS-calculated dispersion coefficients fell within these data points. For the scalar emitted at the top of the channel, apart from the tiny wall-normal RMS velocity fluctuation near the shear-free boundary, the large mean-flow speed suppressed the vertical scalar transport. As a result, its dispersion coefficient was the smallest amongst the emission heights tested within the early plume development and even after the mean plume path switched from the upper to the lower parts of the channel ($x/H \leqslant 9.8$). Moreover, the downward-only turbulent dispersion limited the crosswind scalar transport and the dispersion coefficient.

4.4. *Spatial distribution of mean scalar mixing ratio*

Figure 6 depicts the spatial contours of the mean scalar mixing ratio $\langle\phi\rangle$ on the *x–z* plane in a neutrally stratified channel. The scalar plume generally travelled horizontally in the streamwise direction with unnoticeable meandering. The crosswind coverage of the scalar plume, which is illustrated by the dispersion coefficient along the mean plume path, gradually increased because of the crosswind plume development. On the contrary, obvious scalar-plume meandering, which was illustrated in the form of spatial contours of mean scalar mixing ratio on the *x–z* plane, was observed in the unstably stratified channel (Figure 7).

Under unstable stratification, the mean plume path for the scalar emitted at $z_s/H = 0$ was very close to the wall within the early plume development ($x/H \leqslant 5$, Figure 7(a)). As a result, the maximum mean scalar mixing ratio resided at the wall level. Afterward, the maximum mean scalar mixing ratio followed the mean plume path that ascended to the upper part of the channel. A broad local maximum of mean scalar mixing ratio ($\langle\phi\rangle/\Phi = 1 \times 10^{-3}$) was eventually developed at the shear-free boundary covering $5 \leqslant x/H \leqslant 11.5$. Meanwhile, a broad local minimum of mean scalar mixing ratio ($\langle\phi\rangle/\Phi = 5 \times 10^{-4}$) was developed at the lower part of the channel covering $x \geqslant 6$.

For an elevated emission height in the lower part of the channel at $z_s/H = 0.25$, the spatial contours of mean scalar mixing ratio exhibited minor differences compared with that emitted at $z_s/H = 0$ (Figure 7(b)). Though the mean plume path for the scalar emitted in the lower part of the channel was generally ascending, the spatial contours of mean scalar mixing ratio for the scalar emitted at $z_s/H = 0.25$ showed a mild plume descent right after emission. The descending scalar plume developed a wall-level local maximum of mean scalar mixing ratio ($\langle\phi\rangle/\Phi = 4 \times 10^{-3}$) covering $2.2 \leqslant x/H \leqslant 4.3$. Afterward, the scalar was carried upward to the upper part of the channel. A broad local maximum of mean scalar mixing ratio ($\langle\phi\rangle/\Phi = 4 \times 10^{-3}$) was then developed at the top of the channel covering $5 \leqslant x/H \leqslant 11.7$. Because of the mean plume rise during the early plume development, a local minimum of mean scalar mixing ratio ($\langle\phi\rangle/\Phi = 2 \times 10^{-3}$) was developed on the wall in the far field ($7 \leqslant x/H \leqslant 12$).

The mean plume path for the scalar emitted at the channel centre ($z_s/H = 0.5$) only showed mild scalar-plume meandering on the *x–z* plane (Figure 7(c)). It rose slightly right after emission until $x/H \leqslant 3$. Afterward, it developed a gentle local maximum of mean scalar mixing ratio ($\langle\phi\rangle/\Phi = 3 \times 10^{-3}$) at the shear-free boundary covering $3 \leqslant x/H \leqslant 6$. The scalar was well mixed thereafter with mean scalar mixing ratio $\langle\phi\rangle/\Phi \approx 3 \times 10^{-3}$.

As shown in Figure 7(d), the scalar emitted at $z_s/H = 0.75$ rose slightly right after emission. It developed a local maximum of mean scalar mixing ratio ($\langle\phi\rangle/\Phi = 5 \times 10^{-3}$) at the free-

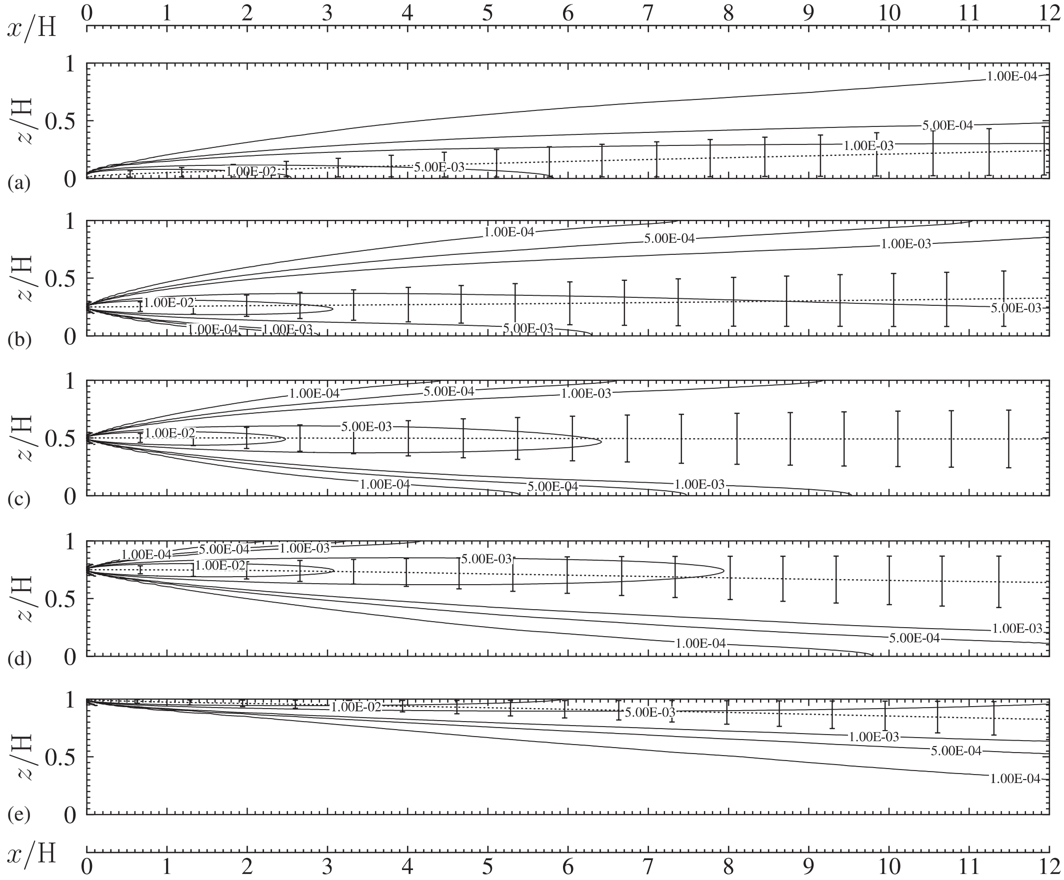

Figure 6. Spatial distribution of mean scalar mixing ratio $\langle\phi\rangle/\Phi$ for scalar emitted at $z_s/H =$: (a) 0, (b) 0.25, (c) 0.5, (d) 0.75, and (e) 1 in an neutrally stratified open channel calculated by the DNS FEM model. Dotted line represents the mean plume path and vertical bars represent the mean plume coverage ($=2\sigma_z/H$) in terms of the dispersion coefficient.

shear boundary covering $2.1 \leqslant x/H \leqslant 3.3$. Afterward, it moved downward (implied by the descending mean plume path) that eventually developed a wall-level local maximum of mean scalar mixing ratio ($\langle\phi\rangle/\Phi = 4 \times 10^{-3}$) extending from $x/H = 7.7$ to the downstream outlet. Meanwhile, a local minimum of mean scalar mixing ratio ($\langle\phi\rangle/\Phi = 2 \times 10^{-3}$) was developed at the shear-free boundary covering $5.8 \leqslant x/H \leqslant 11.2$.

Unlike that emitted at other emission heights, the scalar emitted at $z_s/H = 1$ did not rise, and thus no local maximum of mean scalar mixing ratio was developed at the shear-free boundary. Instead, the scalar was carried downward right after emission that developed a wall-level local maximum of mean scalar mixing ratio ($\langle\phi\rangle/\Phi = 3 \times 10^{-3}$) covering $7 \leqslant x/H \leqslant 10.2$. Because of the plume descent, the mean plume path switched from the upper to the lower parts of the channel for $x/H \geqslant 5$. Meanwhile, a local minimum of mean scalar mixing ratio ($\langle\phi\rangle/\Phi = 5 \times 10^{-4}$) was developed at the shear-free boundary covering $7 \leqslant x/H \leqslant 10.2$.

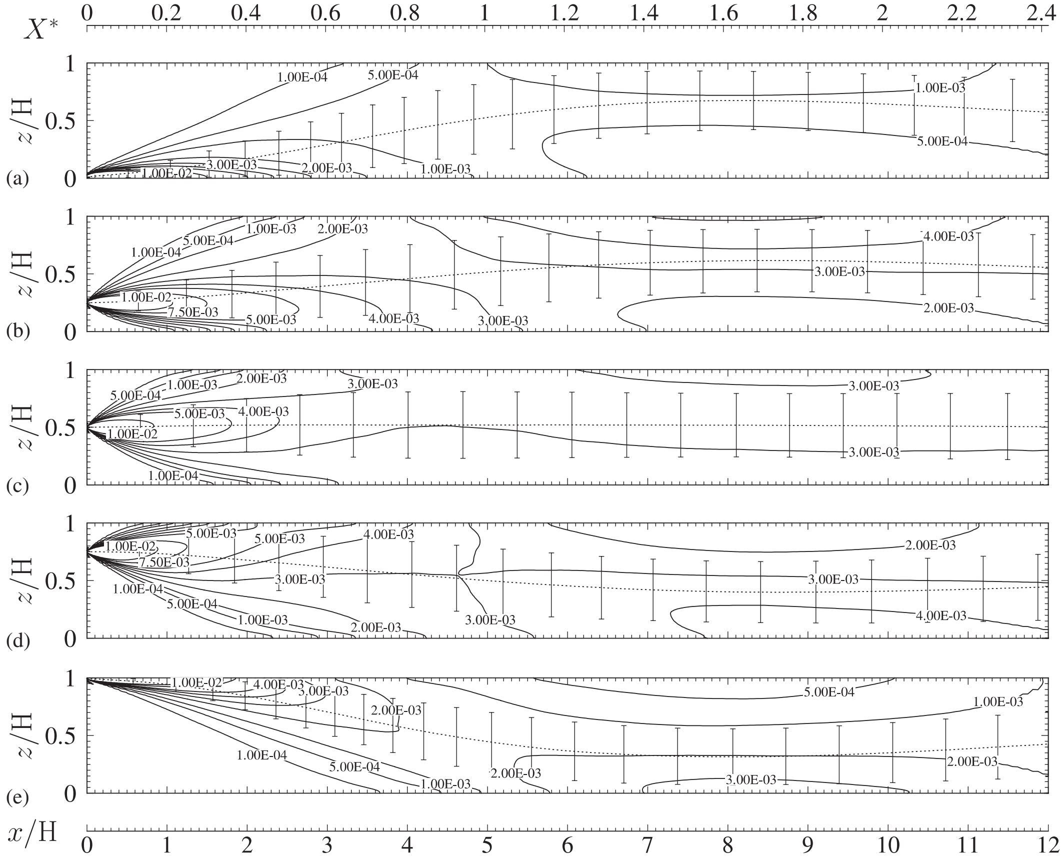

Figure 7. Spatial distribution of mean scalar mixing ratio $\langle\phi\rangle/\Phi$ for scalar emitted at $z_s/H =$: (a) 0, (b) 0.25, (c) 0.5, (d) 0.75, and (e) 1 in an unstably stratified open channel calculated by the DNS FEM model. Dotted line represents the mean plume path and vertical bars represent the mean plume coverage $(= 2\sigma_z/H)$ in terms of the dispersion coefficient.

4.5. Spatial distribution of RMS scalar mixing ratio fluctuation

The spatial contours of the RMS scalar mixing ratio fluctuation $\langle\phi''\phi''\rangle^{1/2}$ for scalar emitted at different heights in a neutrally stratified open channel are depicted in Figure 8. The contours of the RMS scalar mixing ratio fluctuation basically followed those of the mean scalar mixing ratio. It was large near the sources whose value around the sources was greater than that around the downstream outlet by two order of magnitudes. Its crosswind coverage was extending in the wall-normal direction while the plume was developing in the streamwise direction. No noticeable meandering of RMS scalar mixing ratio fluctuation was observed.

On the other hand, the RMS scalar mixing ratio fluctuation for the scalar emitted under unstable stratification showed different characteristics (Figure 9) compared with those under neutral stratification. The spatial-contour meandering in the form of ascending and descending RMS scalar mixing ratio fluctuation was observed for most of the emission heights tested.

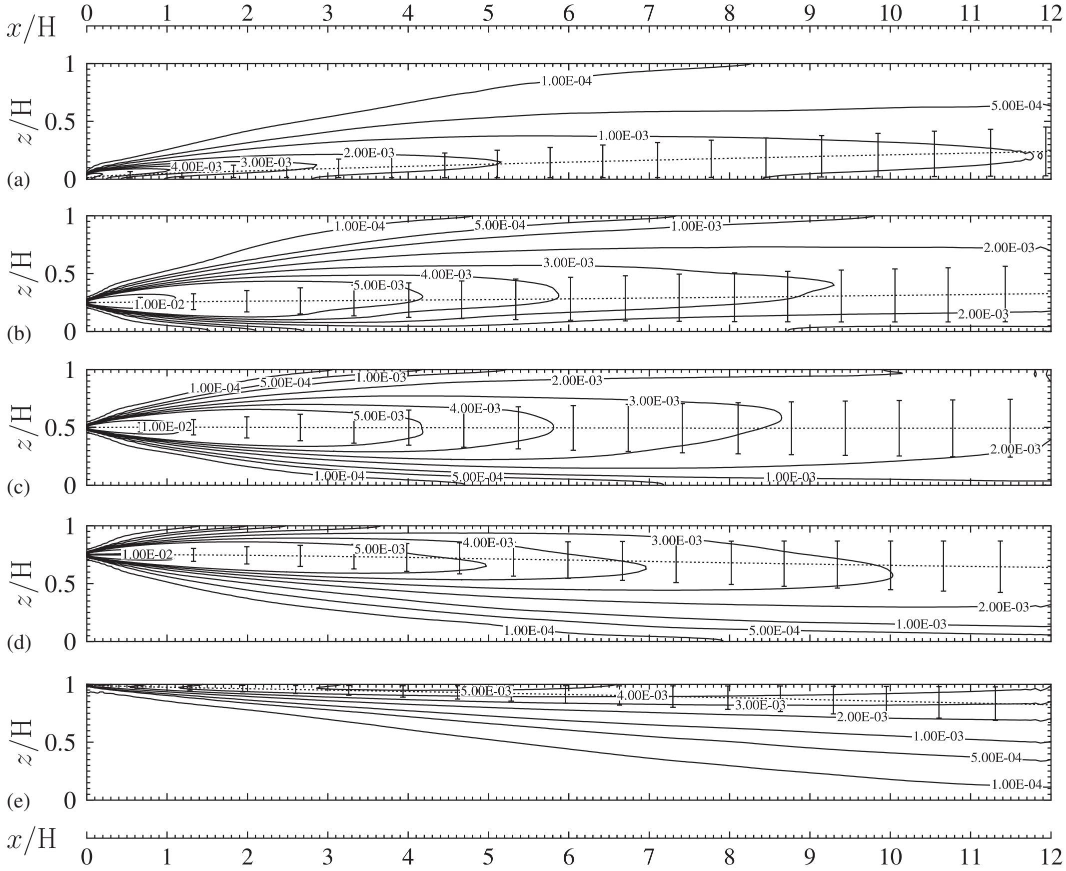

Figure 8. Spatial distribution of RMS scalar mixing ratio fluctuation $\langle \phi'' \phi'' \rangle^{1/2}/\Phi$ for scalar emitted at $z_s/H =$: (a) 0, (b) 0.25, (c) 0.5, (d) 0.75, and (e) 1 in a neutrally stratified open channel calculated by the DNS FEM model. Dotted line represents the mean plume path and vertical bars represent the mean plume coverage ($= 2\sigma_z/H$) in terms of the dispersion coefficient.

As shown previously, a rapid plume rise was observed for the scalar emitted at $z_s/H = 0$ under unstable stratification. Similarly, the RMS scalar mixing ratio fluctuation showed an ascending trajectory right after emission (Figure 9(a)). It rose to the upper part of the channel and then developed a local maximum of RMS scalar mixing ratio fluctuation ($\langle \phi'' \phi'' \rangle^{1/2}/\Phi = 1 \times 10^{-6}$) at the shear-free boundary covering $4 \leqslant x/H \leqslant 5.8$. The high RMS scalar mixing ratio fluctuation then moved along the shear-free boundary toward the downstream outlet and became almost homogeneous eventually.

Unlike those of the mean scalar mixing ratio, the spatial contours of the RMS scalar mixing ratio fluctuation for $z_s/H = 0.25$ did not show noticeable descending trajectory in the near field ($0 \leqslant x/H \leqslant 3$). Instead, the maximum RMS scalar mixing ratio fluctuation travelled horizontally in the near field ($0 \leqslant x/H \leqslant 3$) before rising to the upper part of the channel at $3 \leqslant x/H \leqslant 5$ (Figure 9(b)). Eventually, it developed a local maximum RMS scalar mixing ratio fluctuation ($\langle \phi'' \phi'' \rangle^{1/2}/\Phi = 1 \times 10^{-5}$) at the top of the channel covering $3.2 \leqslant x/H \leqslant 5.8$.

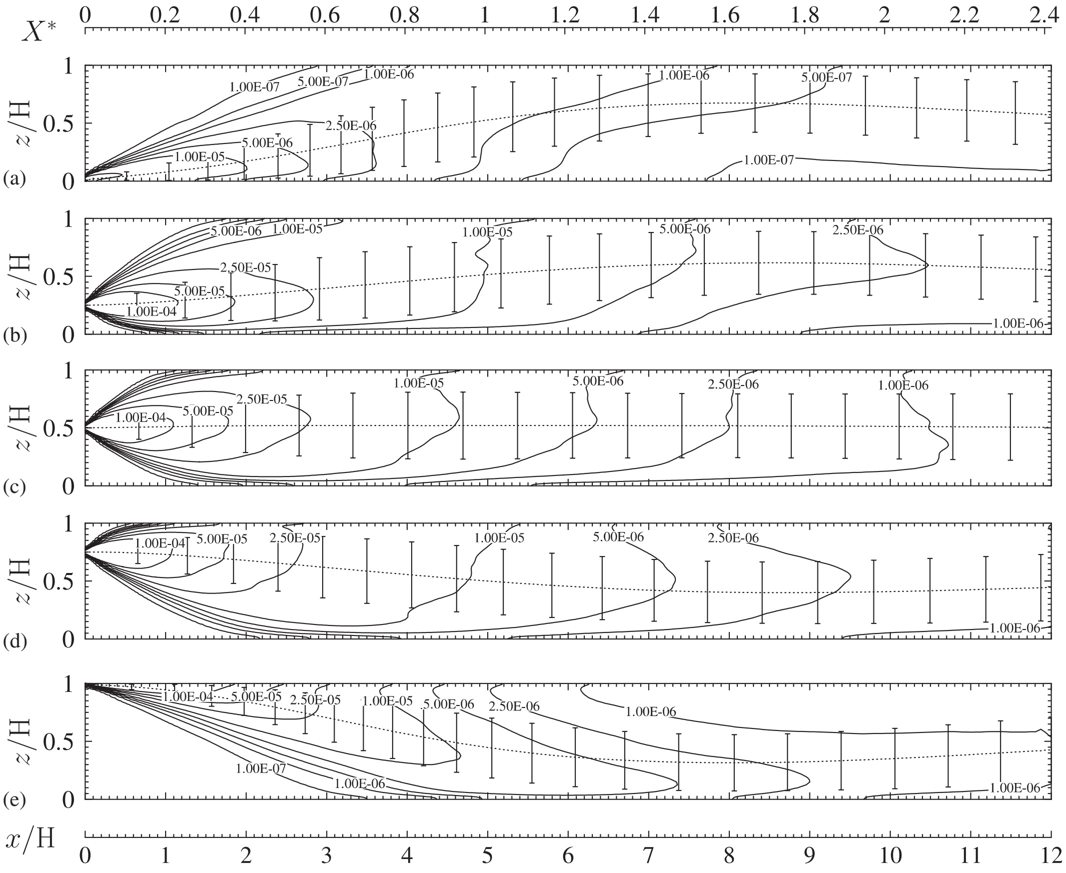

Figure 9. Spatial distribution of RMS scalar mixing ratio fluctuation $\langle\phi''\phi''\rangle^{1/2}/\Phi$ for scalar emitted at $z_s/H =$: (a) 0, (b) 0.25, (c) 0.5, (d) 0.75, and (e) 1 in a unstably stratified open channel calculated by the DNS FEM model. Dotted line represents the mean plume path and vertical bars represent the mean plume coverage ($= 2\sigma_z/H$) in terms of the dispersion coefficient.

Mainly due to the higher mean scalar mixing ratio, the RMS scalar mixing ratio fluctuation in the upper part of the channel was greater than that in the lower part by an order of magnitude. The high RMS scalar mixing ratio fluctuation followed the mean plume path in the upper part of the channel and finally converged toward the channel centre.

For the scalar emitted at the centre of the unstably stratified channel, the high RMS scalar mixing ratio fluctuation generally travelled horizontally in the streamwise direction along the mean plume path (Figure 9(c)). No significant meandering of RMS scalar mixing ratio fluctuation was observed. However, a slight local maximum of RMS scalar mixing ratio fluctuation ($\langle\phi''\phi''\rangle^{1/2}/\Phi = 1 \times 10^{-5}$) was developed at the shear-free boundary covering $2.2 \leqslant x/H \leqslant 4.7$ during the early plume development.

For the scalar emitted at $z_s/H = 0.75$, the spatial characteristics of RMS scalar mixing ratio fluctuation generally followed those of the mean plume path in which the maximum RMS scalar mixing ratio fluctuation travelled horizontally in the streamwise direction in the near field ($0 \leqslant x/H \leqslant 4$, Figure 9(c)). During this travel, a local maximum of RMS scalar mixing ratio fluctuation ($\langle\phi''\phi''\rangle^{1/2}/\Phi = 2.5 \times 10^{-5}$) was developed at the shear-free boundary covering $1.8 \leqslant x/H \leqslant 2.8$. The high RMS scalar mixing ratio fluctuation continued travelling along the shear-free boundary until $x/H = 5.5$. Afterward, it descended slightly toward the channel centre and exhibited quite homogeneous behaviours thereafter.

On the contrary, the RMS scalar mixing ratio fluctuation for the scalar emitted at $z_s/H = 1$ under unstable stratification descended rapidly right after emission (Figure 9(e)). Its descent was the deepest amongst the emission heights tested that almost reached the wall of the channel at $7 \leqslant x/H \leqslant 9$. This decent also developed a mild wall-level local maximum RMS scalar mixing ratio fluctuation ($\langle\phi''\phi''\rangle/\Phi = 2.5 \times 10^{-6}$) covering $4.9 \leqslant x/H \leqslant 8$. Afterward, the high RMS scalar mixing ratio fluctuation rebounded and converged gradually toward the channel centre along the streamwise direction.

4.6. Instantaneous scalar mixing ratio

The previous sections discuss the mean statistical properties that compare the scalar-plume behaviours in the neutrally and unstably stratified channel. Additional perspective of turbulent scalar transport can be obtained by looking into the snapshot of instantaneous spatial contours of velocity fluctuation and scalar mixing ratio. The DNS-calculated snapshots are taken as typical turbulent transport structures.

Figure 10 depicts the spatial contours of instantaneous wall-normal velocity fluctuation w'' on selected x–z and y–z planes under neutral stratification. Parcels of isolated updraft and downdraft were observed that were responsible for the crosswind scalar mixing and plume development. In an isothermal environment, the fluctuating wall-normal velocity was solely driven by mechanical shear that cascaded energy from the mean flow to turbulence. In the aforementioned flow field, the scalar plume under neutral stratification generally travelled horizontally in the streamwise direction with instantaneous plume meandering (in the wall-normal direction) about the mean plume path (Figure 11). This plume meandering was caused by the wall-normal velocity fluctuation w'' that made up the turbulent scalar mixing in the crosswind direction. As a result, the scalar-plume coverage developed with increasing downstream distance. The instantaneous plume meandering did not persist and no noticeable plume meandering was observed in the spatial contours of mean scalar mixing ratio.

The spatial contours of instantaneous wall-normal velocity fluctuation under unstable stratification on selected x–z and y–z planes are illustrated in Figure 12. On top of mechanical shear, the wall-normal velocity fluctuation was enhanced by the buoyancy. Parcels of updraft and downdraft, whose sizes and magnitudes were much greater than those under neutral stratification, were observed. It seemed that some of the updraft and downdraft had organized structure covering almost the whole streamwise extent of the channel. On the contrary, it was unlikely that organized structure of wall-normal velocity fluctuation was observed under neutral stratification. Because of the increased wall-normal velocity fluctuation, enhanced scalar mixing is observed from the spatial contours of the instantaneous scalar mixing ratio under unstable stratification (Figure 13) compared with that in a neutrally stratified one. This finding was reflected from the lower instantaneous scalar mixing ratio in the far field of the channel that was in line with our previous discussion based on the mean quantities of turbulence structure, dispersion coefficients, as well as spatial contours of mean scalar mixing ratio. In fact, enhanced scalar mixing in early plume development under unstable stratification was

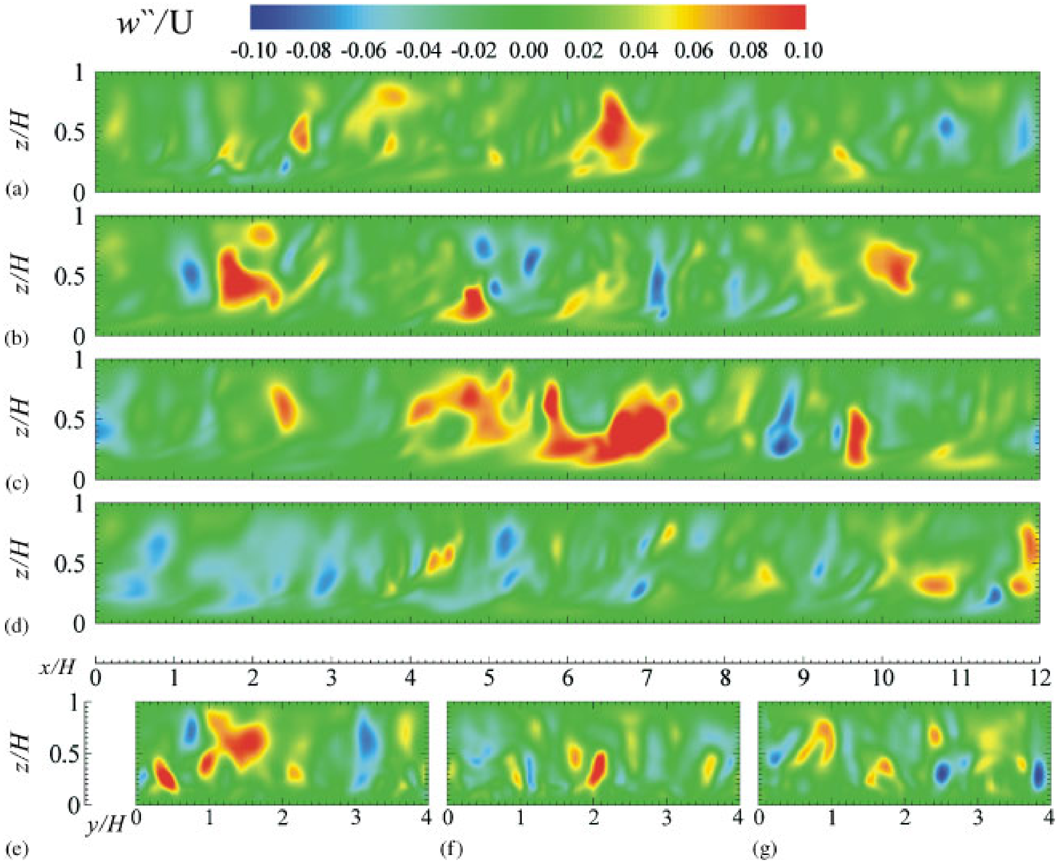

Figure 10. Spatial distribution of instantaneous wall-normal velocity fluctuation w'' on selected planes in a neutrally stratified open channel calculated by the DNS FEM model. x–z planes at $y/H =$: (a) 0, (b) 1, (c) 2, and (d) 3. y–z planes at $x/H =$: (e) 2, (f) 6, and (g) 10.

also observed in the instantaneous scalar properties that was illustrated from the scalar-plume coverage right behind the sources. This early enhanced scalar mixing was particularly obvious for the emission height at $z_s/H = 0.25$ where the wall-normal velocity fluctuation was largest within the channel.

Apart from scalar mixing, scalar-plume meandering in the wall-normal direction under unstable stratification was observed in the instantaneous spatial contours. The scalar emitted in the upper part of the channel showed markedly plume descent at $4 \leqslant x/H \leqslant 5$ (Figures 13(a) and (b)). Similar to the findings based on the mean quantities, the scalar emitted at the channel centre showed least plume meandering amongst the emission heights tested (Figure 13(c)). Moreover, the scalar mixing ratio was fairly homogeneous in most of the channel ($x/H \geqslant 5$). The plume meandering was unnoticeable for the scalar emitted at $z_s/H = 0.25$. Nonetheless, switching of scalar-plume path (high scalar mixing ratio) from the lower to upper parts of the channel is illustrated in Figure 13(d). Close to the downstream outlet of the channel ($x/H \geqslant 8$), the upper part of the channel had higher scalar mixing ratio than that of the lower

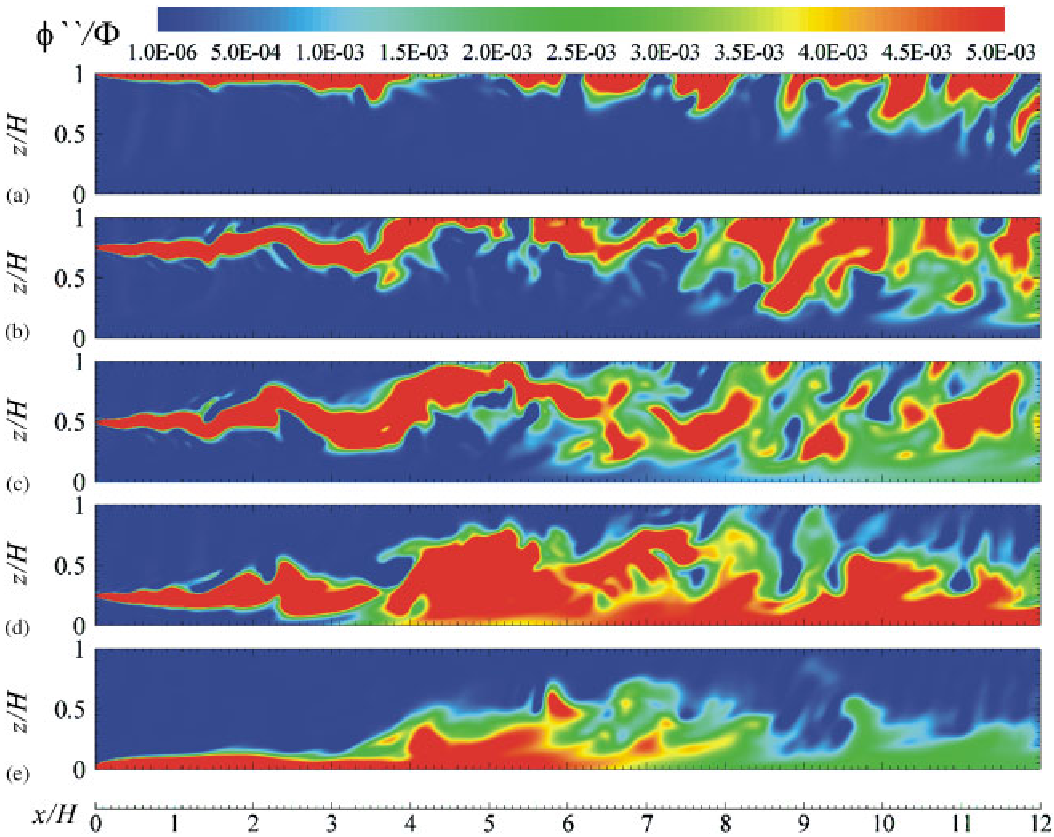

Figure 11. Spatial distribution of mean scalar mixing ratio ϕ/Φ on the x–z plane at $y/H = 2$ for scalar emitted at $z_s/H =$: (a) 1, (b) 0.75, (c) 0.5, (d) 0.25, and (e) 0 in a neutrally stratified open channel calculated by the DNS FEM model.

part. A rapid plume rise was observed from the spatial contours of instantaneous scalar mixing ratio for the scalar emitted at $z_s/H = 0$ (Figure 13(e)).

5. CONCLUSIONS

A DNS FEM code was developed for the numerical modelling of fluid turbulence and passive scalar transport in neutrally and unstably stratified open channels whose mathematical procedures are described in this paper. On top of decoupling the velocity and pressure calculation in incompressible flow, the second-order accurate fractional-step method segregated the solvers for the convection and diffusion terms in the transport equations. The buoyancy term was integrated in time by the explicit first-order accurate Euler scheme. The advection and diffusion terms were integrated in time, respectively, using the explicit third-order accurate Runge–Kutta and the implicit second-order accurate Crank–Nicolson schemes. The Galerkin FEM was used to discretize the spatial domain. An equal-order trilinear interpolating

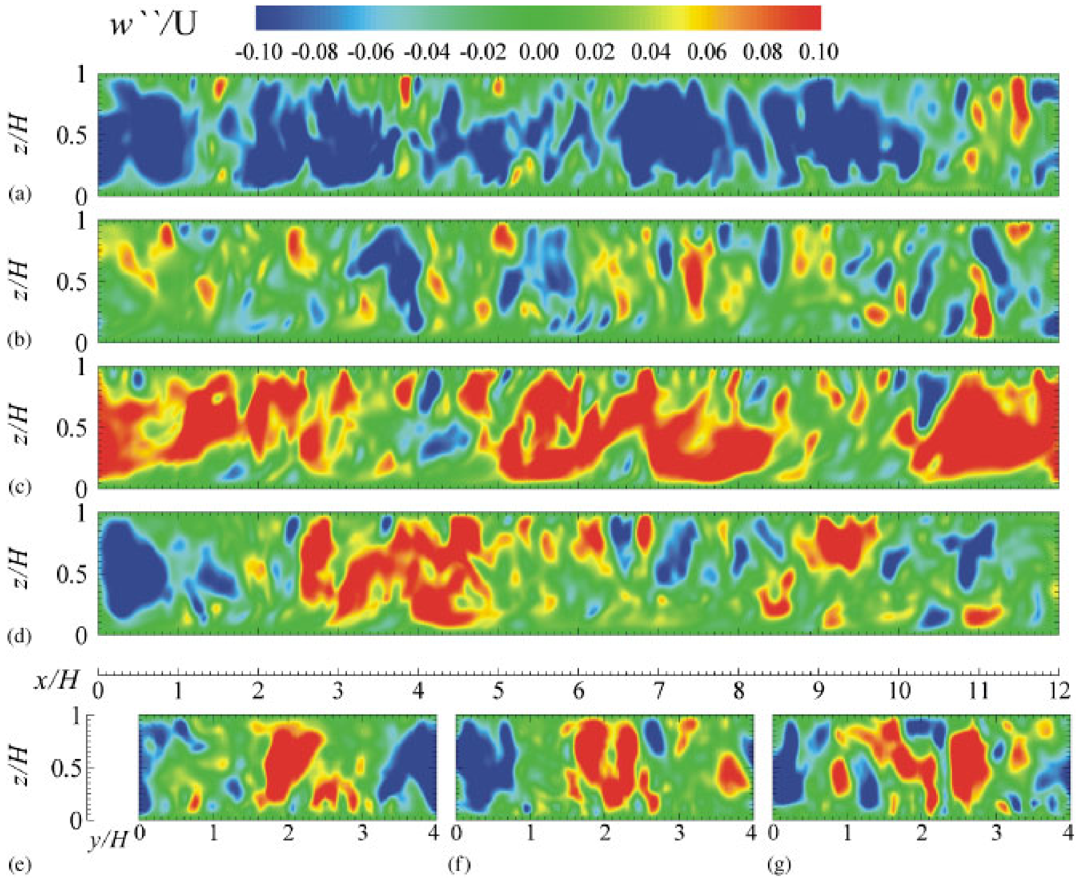

Figure 12. Spatial distribution of instantaneous wall-normal velocity fluctuation w'' on selected planes in an unstably stratified open channel calculated by the DNS FEM model. x–z planes at $y/H =$: (a) 0, (b) 1, (c) 2, and (d) 3. y–z planes at $x/H =$: (e) 2, (f) 6, and (g) 10.

polynomial based on brick elements was employed to approximate the velocity components, pressure, temperature, and scalar mixing ratio. The resulting systems of equations were solved by the conjugate gradient method with the Jacobian preconditioning.

The reliability of the currently DNS FEM model was assessed by comparing its calculated scalar-plume behaviours in unstably stratified open channel with the results available in literature in which their agreement was reasonable. Based on the DNS output, we compared the wall-normal profiles of the mean flow and turbulence under neutral and unstable stratification together with the spatial distributions of mean scalar mixing ratio and RMS scalar mixing ratio fluctuation on the x–z plane. The scalar plume under neutral stratification showed negligible plume meandering. On the other hand, it exhibited remarkable meandering in the form of plume rises and descents under unstable stratification. Comparison of the DNS-calculated dispersion coefficients showed that the crosswind scalar-plume coverage under unstable stratification developed more rapidly than that under neutral stratification.

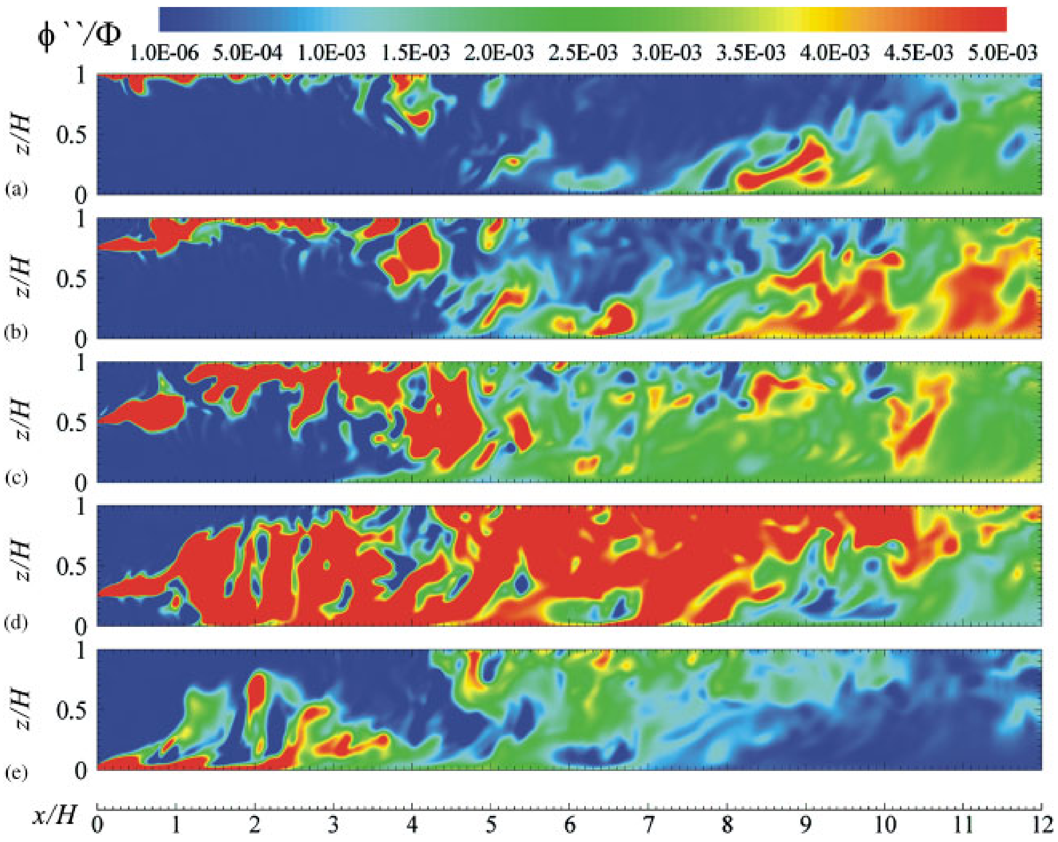

Figure 13. Spatial distribution of instantaneous scalar mixing ratio ϕ/Φ on the x–z plane at $y/H = 2$ for scalar emitted at $z_s/H =$: (a) 1, (b) 0.75, (c) 0.5, (d) 0.25, and (e) 0 in a unstably stratified open channel calculated by the DNS FEM model.

ACKNOWLEDGEMENTS

The authors would like to thank the Computer Centre of the University of Hong Kong for accessing their High Performance Computing Clusters. In particular, we are grateful to Mr Wing-Keung Kwan and Mr Chat-Ming Woo for their generous assistance during the development of the DNS FEM code.

REFERENCES

1. Willis GE, Deardorff JW. A laboratory model for the unstable boundary layer. *Journal of the Atmospheric Sciences* 1974; **31**:1297–1307.
2. Komori S, Ueda H, Ogino F, Mizushina T. Turbulence structure and transport mechanism at the free surface in an open channel flow. *International Journal of Heat and Mass Transfer* 1982; **25**:513–521.
3. Komori S, Ueda H, Ogino F, Mizushina T. Turbulence structure in unstably-stratified open-channel flow. *Physics of Fluids* 1982; **25**:1539–1546.
4. Willis GE, Deardorff JW. A laboratory model of diffusion into the convective planetary layer. *Quarterly Journal of the Royal Meteorological Society* 1976; **102**:427–445.

5. Willis GE, Deardorff JW. A laboratory study of dispersion from an elevated source within a modelled convective planetary boundary layer. *Atmospheric Environment* 1978; **12**:1305–1311.
6. Willis GE, Deardorff JW. A laboratory study of dispersion from a source in the middle of the convectively mixed layer. *Atmospheric Environment* 1981; **15**:109–117.
7. Weil JC, Synder W, Lawson Jr RE, Shipman MS. Experiments on buoyant plume dispersion in a laboratory convection tank. *Boundary-Layer Meteorology* 2002; **102**:367–414.
8. Fedorovich E, Thäter J. A wind tunnel study of gaseous tracer dispersion in the convective boundary layer capped by a temperature inversion. *Atmospheric Environment* 2002; **36**:2245–2255.
9. Fackrell JE, Robins AG. Concentration fluctuations and fluxes in plume from point sources in a turbulent boundary layer. *Journal of Fluid Mechanics* 1982; **117**:1–26.
10. Li JD, Bilger RW. The diffusion of conserved and reactive scalars behind line sources in homogeneous turbulence. *Journal of Fluid Mechanics* 1996; **318**:339–372.
11. Domaradzki JA, Metcalfe RW. Direct numerical simulation of the effects of shear on turbulent Rayleigh–Bénard convection. *Journal of Fluid Mechanics* 1988; **193**:499–531.
12. Liu C-H. Turbulent plane Couette flow and scalar transport at low Reynolds number. *Journal of Heat Transfer* 2003; **125**:988–998.
13. Broglia R, Pascarelli A, Piomelli U. Large-eddy simulations of ducts with a free surface. *Journal of Fluid Mechanics* 2003; **484**:223–253.
14. Kim J, Moin P. Transport of passive scalar in a turbulent channel flow. In *Turbulent Shear Flow 6*, Andre JC, Cousteix J, Durst F, Launder BE, Schmidt FW, Whitelaw JH (eds). Springer: Berlin, 1989; 85–96.
15. Wang WP, Pletcher RH. On the large eddy simulation of a turbulent channel flow with significant heat transfer. *Physics of Fluids* 1996; **8**:3354–3366.
16. Garg RP, Ferziger JH, Monismith SG. Hybrid spectral finite difference simulations of stratified turbulent flows on distributed memory architectures. *International Journal for Numerical Methods in Fluids* 1997; **24**: 1129–1158.
17. Komori S, Nagaosa R, Murakami Y, Chiba S, Ishii K, Kuwahara K. Direct numerical simulation of three-dimensional open-channel flow with zero-shear gas-liquid interface. *Physics of Fluids* 1993; **A5**:115–125.
18. Lu DM, Hetsroni G. Direct numerical simulation of a turbulent open channel flow with passive heat transfer. *International Journal of Heat and Mass Transfer* 1995; **38**:3241–3251.
19. Handler RA, Saylor JR, Leighton RI, Rovelstad AL. Transport of a passive scalar at a shear-free boundary in fully developed turbulent open channel flow. *Physics of Fluids* 1999; **11**:2607–2625.
20. Nagaosa R. Direct numerical simulation of vortex structures and turbulent scalar transfer across a free surface in a fully developed turbulence. *Physics of Fluids* 1999; **11**:1581–1595.
21. Leighton RI, Smith GB, Handler RA. Direct numerical simulation of free convection beneath an air–water interface at low Rayleigh numbers. *Physics of Fluids* 2003; **15**:3181–3193.
22. Livescu D, Jaberi FA, Madnia CK. Passive-scalar wake behind a line source in grid turbulence. *Journal of Fluid Mechanics* 2000; **416**:117–149.
23. Vrieling AJ, Nieuwstadt FTM. Turbulent dispersion from nearby point sources—interference of the concentration statistics. *Atmospheric Environment* 2003; **37**:4493–4509.
24. Choi HG, Choi H, Yoo JY. A fractional four-step finite element formulation of the unsteady incompressible Navier–Stokes equations using SUPG and linear equal-order element methods. *Computer Methods in Applied Mechanics and Engineering* 1997; **143**:333–348.
25. Liu C-H, Leung DYC. Development of a finite element solution for the unsteady Navier–Stokes equations using projection method and fractional-θ-scheme. *Computer Methods in Applied Mechanics and Engineering* 2001; **190**:4301–4317.
26. Barrett R, Berry M, Chan T, Demmel J, Donato J, Dongarra J, Eijkhout V, Pozo R, Romine C, Van der Vorst H. *Templates for The Solution of Linear Systems*: *Building Blocks for Iterative Methods* (2nd edn). SIAM: Philadelphia, PA, 1994.
27. Liu C-H, Leung DYC. Parallel computation of atmospheric pollutant dispersion under unstably stratified atmosphere. *International Journal for Numerical Methods in Fluids* 1998; **26**:677–696.
28. Liu C-H, Leung DYC, Woo C-M. Development of a scalable finite element solution to the Navier–Stokes equations. *Computational Mechanics* 2003; **32**:185–198.
29. Liu C-H, Woo C-M, Leung DYC. Performance analysis of a parallel finite element solution to the direct numerical simulation of fluid turbulence on Linux PC clusters. *Applied Mathematics and Computation* 2005, in press.
30. Liu C-H, Woo C-M, Leung DYC. Performance analysis of a Linux PC clusters using a direct numerical simulation of fluid turbulence code. *International Journal of High Performance Computing Applications* 2005, in press.

31. Kim J, Moin P, Moser R. Turbulence statistics in fully developed channel flow at low Reynolds number. *Journal of Fluid Mechanics* 1987; **177**:133–166.
32. Bech KH, Tillmark N, Alfredsson PH, Andersson HI. An investigation of turbulent plane Couette flow at low Reynolds numbers. *Journal of Fluid Mechanics* 1995; **286**:291–325.
33. Briggs GA. Analytical parameterization of diffusion: the convective boundary layer. *Journal of Climate and Applied Meteorology* 1985; **24**:1167–1186.
34. Liu C-H, Leung DYC. Turbulence and dispersion studies using a three-dimensional second-order closure Eulerian model. *Journal of Applied Meteorology* 2001; **40**:92–112.
35. Dosio A, de Arellano JVG, Holtslag AAM, Builtjes PJH. Dispersion of a passive tracer in buoyancy- and shear-driven boundary layers. *Journal of Applied Meteorology* 2003; **42**:1116–1130.